# Coherent pulse interrogation system for fiber Bragg grating sensing of strain and pressure in dynamic extremes of materials

**George Rodriguez,[1,*] Marcelo Jaime,[1,2] Fedor Balakirev[1,2], Chuck H. Mielke,[1,2] Abul Azad,[1] Bruce Marshall,[3] Brandon M. La Lone,[3] Bryan Henson,[4] and Laura Smilowitz[4]**

[1] *Materials Physics and Applications Division, Los Alamos National Laboratory, Los Alamos, NM 87545, USA*
[2] *National High Magnetic Field Laboratory, Los Alamos, NM 87545 USA*
[3] *Special Technologies Laboratory, National Security Technologies, LLC, Santa Barbara, CA. 93001, USA*
[4] *Chemistry Division, Los Alamos National Laboratory, Los Alamos, NM 87545, USA*
[*] rodrigeo@lanl.gov

**Abstract:** A 100 MHz fiber Bragg grating (FBG) interrogation system is described and applied to strain and pressure sensing. The approach relies on coherent pulse illumination of the FBG sensor with a broadband short pulse from a femtosecond modelocked erbium fiber laser. After interrogation of the FBG sensor, a long multi-kilometer run of single mode fiber is used for chromatic dispersion to temporally stretch the spectral components of the reflected pulse from the FBG sensor. Dynamic strain or pressure induced spectral shifts in the FBG sensor are detected as a pulsed time domain waveform shift after encoding by the chromatic dispersive line. Signals are recorded using a single 35 GHz photodetector and a 50 G Samples per second, 25 GHz bandwidth, digitizing oscilloscope. Application of this approach to high-speed strain sensing in magnetic materials in pulsed magnetic fields to ~150 T is demonstrated. The FBG wavelength shifts are used to study magnetic field driven magnetostriction effects in $LaCoO_3$. A sub-microsecond temporal shift in the FBG sensor wavelength attached to the sample under first order phase change appears as a fractional length change (strain: $\Delta L/L<10^{-4}$) in the material. A second application used FBG sensing of pressure dynamics to nearly 2 GPa in the thermal ignition of the high explosive PBX-9501 is also demonstrated. Both applications demonstrate the use of this FBG interrogation system in dynamical extreme conditions that would otherwise not be possible using traditional FBG interrogation approaches that are deemed too slow to resolve such events.

**OCIS codes:** (060.3735) Fiber Bragg gratings; (000.2170) Equipment and techniques; (060.2370) Fiber optics sensors; (060.2300) Fiber measurements; (120.5475) Pressure measurement; (320.7160) Ultrafast technology.

## References and links

1. E. Udd, ed., *Fiber Optic Sensors, An Introduction for Engineers and Scientists* (John Wiley & Sons Ltd, 1991).
2. J. M. Lopez-Higuera, ed., *Handbook of Optical Fibre Sensing Technology* (John Wiley & Sons Ltd, 2002).
3. E. Udd, "An overview of fiber-optic sensors," Rev. Sci. Instrum. **66**(8), 4015–5030 (1995).
4. S. J. Mihailov, "Fiber Bragg grating sensors for harsh environments," Sensors (Basel) **12**(12), 1898–1918 (2012).
5. G. Rodriguez, R. L. Sandberg, B. M. Lalone, B. Marshall, M. Grover, G. D. Stevens, and E. Udd, "High pressure sensing and dynamics using high speed fiber Bragg grating interrogation systems," SPIE **9098**, 90980C (2014).
6. R. L. Sandberg, G. Rodriguez, L. L. Gibson, D. M. Dattelbaum, G. D. Stevens, M. Grover, B. M. Lalone, and E. Udd, "Embedded optical probes for simultaneous pressure and temperature measurement of materials in extreme conditions," J. Phys. Conf. Ser. **500**(14), 142031 (2014).
7. A. Ravid, E. Shafir, S. Zilberman, G. Berkovic, B. Glam, G. Appelbaum, and A. Fedotov Gefen, "Fibre Bragg grating sensor for shock wave diagnostics," J. Phys. Conf. Ser. **500**(14), 142029 (2014).
8. E. Udd, G. Rodriguez, and R. L. Sandberg, "High speed fiber grating pressure sensors," SPIE **9098**, 90980B (2014).

#237107 - $15.00 USD
Received 7 Apr 2015; accepted 18 May 2015; published 21 May 2015

9. R. Daou, F. Weickert, M. Nicklas, F. Steglich, A. Haase, and M. Doerr, “High resolution magnetostriction measurements in pulsed magnetic fields using fiber Bragg gratings,” Rev. Sci. Instrum. **81**(3), 033909 (2010).
10. Y. Nakazaki and S. Yamashita, “Fast and wide tuning range wavelength-swept fiber laser based on dispersion tuning and its application to dynamic FBG sensing,” Opt. Express **17**(10), 8310–8318 (2009).
11. S. Kim, O.-J. Kwon, H.-S. Lee, C.-S. Kim, and Y.-G. Han, “Long distance fiber Bragg grating strain sensor interrogation using a high speed Raman-based Fourier domain mode-locked fiber laser with recycled residual Raman pump,” Opt. Express **21**(11), 13402–13407 (2013).
12. H. Xia, C. Wang, S. Blais, and J. Yao, “Ultrafast and precise interrogation of fiber Bragg grating sensor based on wavelength-to-time mapping incorporating higher order dispersion,” IEEE J. Lightw. Technol. **28**(3), 254–261 (2010).
13. M. Lai, D. Karalekas, and J. Botsis, “On the effects of the lateral strains on the fiber Bragg grating response,” Sensors (Basel) **13**(2), 2631–2644 (2013).
14. M. G. Xu, L. Reekie, Y. T. Chow, and J. P. Dakin, “Optical in-fibre grating high pressure sensor,” Electron. Lett. **29**(4), 398–399 (1993).
15. Q. Chen, P. Lu, Q. Y. Chen, and P. Liu, “Fiber Bragg gratings and their applications as temperature and humidity sensors,” in *Atomic, Molecular and Optical Physics*, ed. L.T. Chen (Nova Science Publishers, 2008).
16. O. V. Mazurin, *Handbook of Glass Data,* Vol. 1, 75 (Elsevier, 1983).
17. V. Zapf, M. Jaime, and C. D. Batista, “Bose-Einstein condensation in quantum magnets,” Rev. Mod. Phys. **86**(2), 563–614 (2014).
18. M. Jaime, R. Daou, S. A. Crooker, F. Weikert, A. Uchida, A. E. Feiguin, C. D. Batista, H. A. Dabkowska, and B. D. Gaulin, “Magnetostriction and magnetic texture to 100.75 Tesla in frustrated $SrCu_2(BO_3)_2$,” Proc. Natl. Acad. Sci. U.S.A. **109**(31), 12404–12407 (2012).
19. M. M. Altarawneh, G.-W. Chern, N. Harrison, C. D. Batista, A. Uchida, M. Jaime, D. G. Rickel, S. A. Crooker, C. H. Mielke, J. B. Betts, J. F. Mitchell, and M. J. R. Hoch, “Cascade of magnetic field induced spin transitions in $LaCoO_{3,}$,” Phys. Rev. Lett. **109**(3), 037201 (2012).
20. R. R. J. Maier, W. N. MacPherson, J. S. Barton, J. D. C. Jones, S. McCulloch, and G. Burnell, “S, McCulloch, and G. Burnell, “Temperature dependence of the stress response of fibre Bragg gratings,” Meas. Sci. Technol. **15**(8), 1601–1606 (2004).
21. E. Udd and J. Benterou, “Improvements to high-speed monitoring of events in extreme conditions using fiber Bragg grating sensors,” SPIE **8370**, 83700L (2014).
22. E. Shafir, S. Zilberman, A. Ravid, B. Glam, G. Appelbaum, A. F. Gefen, Y. Saadi, N. Shafir, and G. Berkovic, “Comparison to FBG responses to static and dynamic pressures,” SPIE **9157**, 915713 (2014).
23. C. H. Mielke and B. M. Novac, “Experimental and numerical studies of megagauss magnetic-field generation at LANL-NHMFL,” IEEE Trans. Magn. **38**(8), 1739–1749 (2010).
24. V. V. Platanov, Y. B. Kudasov, M. P. Monakhov, and O. M. Tatsenko, “Magnetically induced phase transitions in $LaCoO_3$ in fields of up to 500 T,” Phys. Solid State **54**(2), 279–282 (2012).
25. B. F. Henson, L. Smilowitz, J. J. Romero, B. W. Asay, M. Elert, M. D. Furnish, W. W. Anderson, W. G. Proud, and W. T. Butler, “Modeling thermal ignition and the initial conditions for internal burning in PBX 9501,” AIP Conf. Proc. **1195**, 257–262 (2009).
26. L. Smilowitz, B. F. Henson, G. Rodriguez, and M. Richard Sandberg, Holmes, A. Novak, D. Oschwald, and E. Baca, “Following reaction progress from thermal decomposition to ignition and internal burning,” presented at the Fifteenth International Detonation Symposium, San Francisco, California, USA, 13–18 Jul. 2014.
27. L. Smilowitz, B. F. Henson, J. J. Romero, B. W. Asay, A. Saunders, F. E. Merrill, C. L. Morris, K. Kwiatkowski, G. Grim, F. Mariam, C. L. Schwartz, G. Hogan, P. Nedrow, M. M. Murray, T. N. Thompson, C. Espinoza, D. Lewis, J. Bainbridge, W. McNeil, P. Rightley, and M. Marr-Lyon, “The evolution of solid density within a thermal explosion II. Dynamic proton radiography of cracking and solid consumption by burning,” J. Appl. Phys. **111**(10), 103516 (2012).
28. L. Smilowitz, B. F. Henson, M. Holmes, A. Novak, D. Oschwald, P. Dolgonos, and B. Qualls, “X-ray transmission movies of spontaneous dynamic events,” Rev. Sci. Instrum. **85**(11), 113904 (2014).
29. L. Smilowitz, B. F. Henson, J. J. Romero, and D. Oschwald, “Thermal decomposition of energetic materials viewed via dynamic x-ray radiography,” Appl. Phys. Lett. **104**(2), 024107 (2014).
30. J. W. Forbes, F. Garcia, C. M. Tarver, P. A. Urtiew, D. W. Greenwood, and K. S. Vandersall, “Pressure wave measurements during thermal explosion of HMX-based high explosives,” presented at the Twelfth International Detonation Symposium, San Diego, California, USA, 13–16 Aug. 2002.

---

## 1. Introduction

Fiber Bragg grating (FBG) based sensors are used for research and commercial based strain, temperature, and pressure sensing. They provide a very good basis for distributed sensing because their operational modality is rooted in multiplexing approaches from optical telecommunications technology [1–3]. However, much less is known about their performance in high-speed dynamic events that push the limits of FBG sensing to extreme environments under sub-microsecond transient loading conditions where both sensor and readout rates demand performance currently unavailable commercially [4–8]. For example, there are sensing applications that require readout rates of the FBG spectrum that are higher than the current multi-kHz range of spectrometers based on linear detector arrays [9]. Other high speed FBG interrogation systems rely on frequency swept laser sources capable of reaching the tens of kHz to MHz interrogation rate level [10,11]. Briefly, our approach capitalizes on similar work published by Xia, et al [12]. We utilize a broadband pulse from an ultrafast modelocked fiber laser to probe the FBG. The spectral response of the FBG is then mapped into time using a long dispersive fiber on a single element photodetector coupled to a transient digitizer. This method allows us to capture the optical spectrum of the FBG sensor at the repetition rate of the laser source (100 MHz). Using this approach, we find that FBG strain and pressure sensing can now be performed on experiments where 10 ns resolution is highly desired.

In this paper, we describe our coherent pulse 100 MHz FBG interrogation system in detail, and then provide two example experiments that directly benefit from the added time resolution. In the first example, we apply the technique to a series of proof-of-principle magnetostriction measurements on the National High Magnetic Field Laboratory (NHMFL) single-turn coil magnet system to 150T. In these experiments a single FBG sensor was epoxied to a crystal of the magnetic insulating perovskite cobaltite $LaCoO_3$ (LCO), and the dynamic strain produced by magnetostriction in the crystal was observed using the 100 MHz coherent pulse fiber Bragg interrogation method. In the second example, we embed the FBG sensor in small samples of polymer-bonded high explosives (PBX-9501) and measure the *in-situ* dynamic pressure response resulting from thermal ignition. In both examples, we show that extreme material dynamics are resolved using this FBG sensing approach.

## 2. Fiber Bragg grating interrogation system description

Standard bare single-mode fiber with 1-mm-long or 2-mm-long FBG sensors were procured from a variety of fiber grating vendors: Micron Optics Inc. (Atlanta, Georgia, USA), O-E Land Inc. (Montreal, Quebec, Canada), and Timbercon Inc.(Tualatin, Oregon, USA). All the FBG sensors used were uniform (i.e., unchirped) single wavelength (1550 nm) gratings written on Corning SMF28e polyimide coated single mode fiber. The reflection signal strength and bandwidth properties of each FBG sensor is dependent on grating length. An optical backscatter reflectometer, OBR (Luna Innovations OBR4600), was used to characterize each sensor spectrum and reflection efficiency. In Fig. 1(a), we show a typical return spectrum from an FBG located at the tip of a meter long pigtailed fiber. After characterization with the OBR, the fiber is cut so that the FBG at the very tip of the open end (unconnectorized end) is exposed before placement onto the $LaCO_3$ crystal or PBX-9501 for each experiment.

The strain (and temperature) response of an FBG sensor for magnetostriction measurements was recently described in a paper by Daou, *et al.* [9] where the fractional Bragg wavelength ($\lambda_B$) shift response to strain ($\varepsilon_z$) along the fiber axis and temperature change ($\Delta T$) was given as:

$$\frac{\Delta\lambda_B}{\lambda_B} = \left(1 - \frac{n^2}{2}\left(p_{12} - v\left(p_{11} + p_{12}\right)\right)\right)\varepsilon_z + \left(\alpha\left(T\right) + \frac{1}{n}\frac{dn}{dT}\right)\Delta T, \quad (1)$$

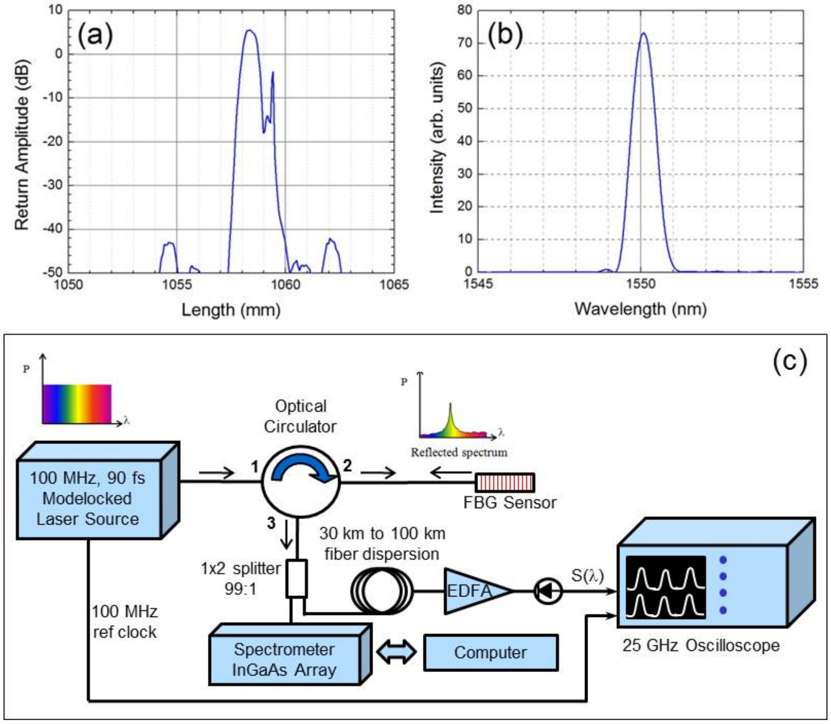

Fig. 1. A typical 1550-nm 1-mm long uniform fiber Bragg grating (a) return signal amplitude and (b) intensity spectrum is shown as recorded by the OBR (optical backscatter reflectometer). An illustration of the coherent pulse FBG interrogation system is shown in (c).

where, $\lambda_B = 2n\Lambda$. The grating pitch and fiber optical index are $\Lambda$ and $n$, respectively. The bracketed factored in front of the strain term consists of the relevant strain-optic photoelastic coefficient terms ($p_{ij}$ ), Poisson's ratio ($v$), and the optical index. The values of the various terms are tabulated in the literature [13,14]: $p_{11}$=0.121, $p_{12}$=0.270, n=1.468 for SMF28e fiber at 1550 nm, and $\nu$=0.19. The collection of these terms yields a value of 0.7 for the computed factor in front of the strain term. Therefore, the strain coefficient (in terms of wavelength shift per unit of micro-strain) for SMF28e fiber is 1.2 pm/με at 1550 nm. The temperature dependence of the Bragg wavelength shift is dominated by the thermo-optic coefficient of the index, $1/n\ dn/dT = 7.0\text{-}7.6\text{x}10^{-6}\ °\text{C}^{-1}$ [14], which is approximately an order of magnitude greater than the thermal expansion coefficient, $\alpha = 5.5\text{x}10^{-7}\ °\text{C}^{-1}$ [15,16]. The temperature coefficient (in terms of wavelength shift per degree Celsius) for SMF28e fiber is ~12 pm/°C. Fortunately, in the course of pulsed magnetic field experiments, the sample temperature remains essentially unchanged at near liquid He temperatures. There is usually a very small self-heating and/or magnetocaloric effect (MCE) [17], but the temperature term in Eq. (1) can be neglected [9,17–19].

The equation relating the fractional Bragg wavelength shift to pressure, P, is done using the relation of the pressure to the strain term [14]:

$$\varepsilon_z = -\left(\frac{1-2v}{E}\right)\text{P}, \tag{2}$$

where, E is Young's modulus. Young's modulus for SMF28e fiber is E~70 GPa [14,20], and the calculated pressure induced shift is -11 pm/MPa. This is several times higher than what experimental isotropic hydrostatic tests yield where values in the -3.5 to -4 pm/MPa have been measured in hyperbaric chamber tests [14,21,22]. This discrepancy has been identified and attributed to additional contributions from the lateral strains where the three dimensionality of the strain field in isotropic measurements change the axisymmetric response that was assumed in Eq. (1) using a Poisson relation $\varepsilon_x=\varepsilon_y=-\nu\varepsilon_z$ [13]. Instead, for the case of isotropic hydrostatic pressure measurements, biaxiality includes large axial and transverse strains and changes Eq. (1) to account for significant transverse strain:

$$\frac{\Delta\lambda_B}{\lambda_B}=-\left(1-\frac{n^2}{2}\left(p_{12}+B\left(p_{11}+p_{12}\right)\right)\right)\left(\frac{1-2\nu}{E}\right)\mathrm{P}+\left(\alpha\left(T\right)+\frac{1}{n}\frac{dn}{dT}\right)\Delta T\,, \quad (3)$$

where, B= $(\varepsilon_x/\varepsilon_z)$ is called the biaxiality ratio [13]. A finite element model was used to compare with isotropic pressure measurements using B=1, and good agreement was achieved with yielding a calculated pressure calibration of -4 pm/MPa. In FBG sensing applications of Section 3, the magnetostriction strain experiments are 1D, so Eq. (1) is valid. In the thermal explosion pressure measurements, we assert that the pressure dynamics are slow enough that isotropic quasi-static pressures are attained and Eq. (3) is applicable. This would not be true of the pressure was derived from 1D shock wave traveling in a direction normal or parallel to the FBG axis.

The coherent pulse FBG interrogation system is illustrated in Fig. 1(c). Modelocked 90-fs pulses from an Er fiber laser (Menlo Systems T-Light Laser) centered at 1560 nm with a 100 MHz repetition rate are launched into a single mode fiber (SMF28e) based system. The laser delivers broadband (1510 nm–1610 nm at the -10 dB points) pulses that are sufficient for illuminating FBGs of various types and wavelength channels. For these studies, single wavelength non-chirped FBGs between 1550 nm and 1560 nm were used. Laser pulses travel through a super wide band (S+C+L Band) 3-port circulator, illuminate the FBG sensor, and then exit port 3 to a 1x2 99:1 splitter. One percent of the return light from the FBG sensor was directed to a FBG interrogator volume grating based spectrometer (Bayspec Inc. model FBGA-IRS-F-1525-1565-FA) with a 512-element InGaAs linear arrayed detector. The majority (99%) of FBG return light after the 1x2 splitter was sent along a chromatic dispersive element consisting of 30 km to 100 km spool of SMF28e fiber. The length of fiber used depended on the amount of time stretching and wavelength resolution desired since the stretched pulse translates into group delay wavelength mapping of the dispersed pulse into time for recording. After chromatic dispersion, time stretched pulse signals were amplified using a C-Band erbium doped fiber amplifier (EDFA model NP200C-PR from Nuphoton Technologies) to boost the power losses introduced by the fiber spool to the few dBm level. A 35 GHz InGaAs photodetector (Newport, Inc. model 1474A) converted the optical pulse train to electrical pulses for recording on a single channel of a 25 GHz, 50 GS/sec digitizing oscilloscope (Tetronix, Inc. DPO72004C). In addition to recording the optical time domain pulse train from the FBG sensor, a reference clocking signal directly from the laser is also recorded. The average dispersion constant for SMF28e fiber is 0.0167 ns/(nm-km). If a 100 km spool is used for chromatic dispersion, the effective spectral band between modelocked pulses (*i.e.*, 10 ns inter-pulse period) is 5.99 nm.

In Fig. 2 we show sample plots of time domain signals recorded at 50 GS/sec. In Fig. 2(a) the plot shows a time window between zero and 0.1 μsec of the typical FBG signal pulse train (after 60 km of fiber) and the laser reference clock signal. The FBG time domain signal in Fig. 2(a) is the FBG grating whose properties were shown in Fig. 1. The plot in Fig. 2(b) is a zoomed in time domain signal showing the corresponding wavelength in the top axis of the plot. Spectral resolution of the FBG interrogation system in the time domain signal is principally determined by the following: amount of chromatic dispersion, photodetector speed, oscilloscope sampling rate and analog bandwidth. For 60 km of fiber, 35 GHz detector, 50 GS/sec, and 25 GHz bandwidth, resolution is approximately 50 ps corresponding 200 effective wavelength points in a 10 ns time window (equivalent to a 9.98 nm wavelength window) is 9.98 nm/200 = 50 pm. The simplest method to improve spectral resolution is by

#237107 - $15.00 USD Received 7 Apr 2015; accepted 18 May 2015; published 21 May 2015

increasing the chromatic dispersion. To date, we have used 100 km in some of our experiments without too much degradation in signal to noise. However, with losses from the fiber spool at 0.2 dB/km, the limitation using this approach to improve resolution is determined by the input noise ceiling of the EDFA, we expect that to be at 150 km to 200 km lengths. Furthermore, the addition of fiber also decreases the observable inter-pulse time/wavelength window.

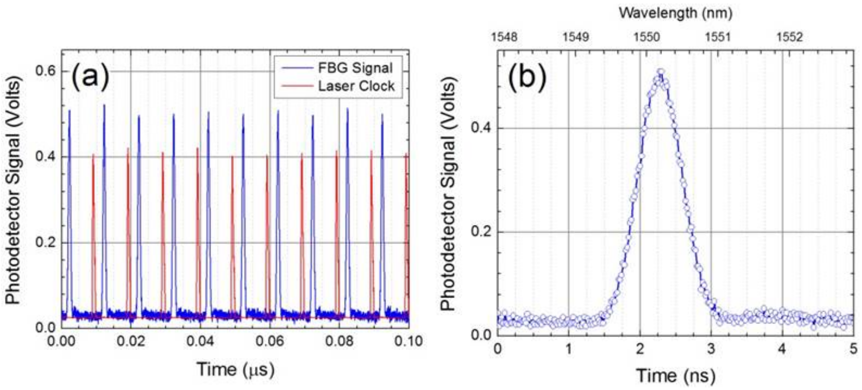

Fig. 2. A very short 100 ns segment of the oscilloscope recorded FBG and laser clock temporal waveforms are shown in (a). A zoomed in line-symbol plot of a single FBG waveform is shown in (b). The top axis in (b) is the wavelength mapped axis after conversion using the chromatic dispersion constant for a fiber spool length of 60 km.

Analysis of the time domain FBG waveforms was done using a Labview program. Record lengths can be extremely long as some of the oscilloscopes have memory capacity of 62.5 MPts per channel. At 50 GS/sec, transient events of up to 1.25 ms are recordable. To analyze an FBG record, both the laser ref clock and FBG signals are read in by the FBG data analysis program. The laser clock waveform is then shifted in time so that the initial peaks of the laser clock are temporally aligned with the FBG pulse waveform. Then using a scanning time window and the peak positions of the laser clock waveform, time slices of a full laser clock period (approximately, $\Delta t = \pm 5$ ns on each side of a laser clock pulse) are extracted from FBG waveform using the laser clock peak positions as the local time zero point. The time slice period (~10 ns) is equal to the inverse repetition rate of the laser. Extraction of the time slices in the FBG waveform is done for the entire record and then into array form such that the time slice window contains a time/spectral readout information while the time axis points are determined from the laser clock peaks that occur at 100 MHz (every 10 ns). Thus, temporal resolution is determined by the laser clock period. A sample plot illustrating the post-processing data result is shown in the plot of Fig. 3. It contains a FBG time domain plot for a 1-mm-long 1555nm FBG strain dilation measurement on the magnetic perovskite $LaCoO_3$ sample using a pulsed-power driven magnetic field to 150 T. The response of the crystal is due to linear magnetostriction resulting from the field alignment along the crystal *c*-axis (see description in next section) when the pulsed magnet is turned on for only a brief instant (~6 µs). The resulting effect is a positive shift in time of the FBG time domain response as the sensor becomes elongated since it is bonded to the sample. After the initial impulse from the field, oscillatory ringing in the FBG sensor signals is observed as the sudden elongation in the crystal drives an acoustic wave with a period equal to twice the sound transit time in the sample. Conversion to a wavelength shift in the FBG sensor is done using the dispersion coefficient factor of 0.0167 ns/(nm-km) and the chromatic dispersive length of the fiber (50.036 km) for the experiment. The corresponding $\Delta\lambda$ wavelength shift is shown as the right ordinate labels in Fig. 3.

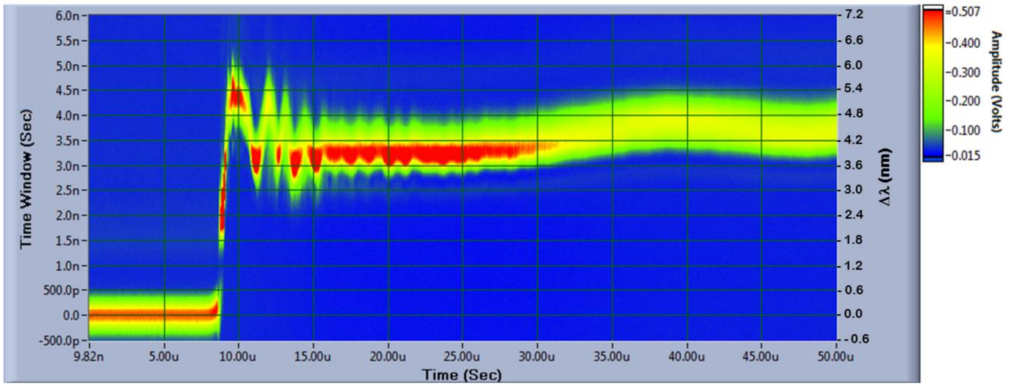

Fig. 3. Example plots of processed coherent time domain FBG waveform data from a pulsed magnetic field (150 T) driven magnetostriction strain experiment on the 2-mm long magnetic perovskite LaCoO$_3$ system followed by launch an acoustic wave after elongation of the sample. We show a time-time plot of the 1555 nm 1-mm FBG sensor versus for 50.036 km of dispersion. The left ordinate axis is a window of 6.5 ns within one laser clock period time slice (10 ns), and the abscissa axis is the event time beginning from the trigger of the NHMFL single-turn capacitor bank and has not been time corrected for the various delays in the signal and trigger paths. Conversion of the left ordinate time axis of into FBG wavelength shift yields a λ-shift (Δλ vs. t) time plot as shown in the right ordinate axis labels. A positive shift to longer wavelength indicates that the strain resulted in elongation of the sensor/sample combination. A mean FBG wavelength shift of over $\overline{\boldsymbol{\Delta\lambda}} \geq \boldsymbol{+4}$ nm is observed.

## 3. Applications

### *3.1 Strain: fiber Bragg grating dilatometry of materials in ultra-high magnetic fields*

Fiber Bragg grating based magnetostriction measurements of materials in high magnetic fields have only recently been demonstrated [9,18,19] to provide valuable strain based measurements of field-induced magnetic phenomena. Direct coupling to lattice changes in quantum paramagnets and antiferromagnets have been of interest because the lattice response directly measures the spin effects using the magnetic field amplitude as a tuning parameter to observe quantum processes. In 2012, the pulsed field facility at the National High Magnetic Field Laboratory (NHMFL) reached a field strength of 100.75 T in motor generator driven long pulse (5 ms) non-destructive magnetic field where FBG magnetostriction measurements [18] on a sample of the antiferromagnet crystal $SrCu_2(BO_3)_2$ were used to study spin-lattice correlation effects. Approaches to FBG strain based magnetostriction measurements, however, become exceedingly difficult when trying to use the next level of pulsed field magnets, namely single-turn coils, capable of 150T – 300T. Although destructive for the magnet itself (normally not so to the sample under study), these capacitor bank-based pulsed capabilities [23] enable exploration of magnetic phenomena to previously inaccessible regimes. Diagnostic challenges are, however, significant since strain sensitive FBG's must be interrogated at speeds that are fast compared to the few µsec-long magnetic field pulses of the single-turn coil magnet to be able to resolve the sample's strain dynamics. Here we demonstrate that our 100 MHz coherent pulse FBG interrogation system is indeed capable of time resolving the magnetostriction strain dynamics.

The current-voltage performance characteristics of the single-turn capacitor driven pulsed magnet at the NHML in Los Alamos has been previously described [23]. A photograph of the facility is shown in Fig. 4(a). Briefly, a maximum voltage of 60 kV and a peak current of 4.5 MA is discharged in a sinusoidal shaped current pulse with a peak current rise time of 2.3 µs. Stored energy in the capacitor bank is delivered to a single-turn coil (Fig. 4(b)) where the current generated magnetic field (H) is setup along the z-axis of the coil. The dimensions of the OHFC copper coil are: 0.625" outside diameter, 0.125" wall thickness, and 10 mm long. A few mm axial region in the center of the coil produces a uniform field where the sample was placed. In addition, a flowing liquid He tubular cryogenic system was used to cool and maintain samples at T = 4K. A photograph of a sample ($LaCoO_3$) with an epoxy attached 1-mm 1550 nm FBG sensor and B-dot loop is shown in Fig. 4(c). The so-called B-dot coil is used as an *in-situ* probe for the magnetic field at the sample. In Fig. 4(d) is a plot of the typical H field waveform measured for an experiment. Peak field at the sample is 152.7 T.

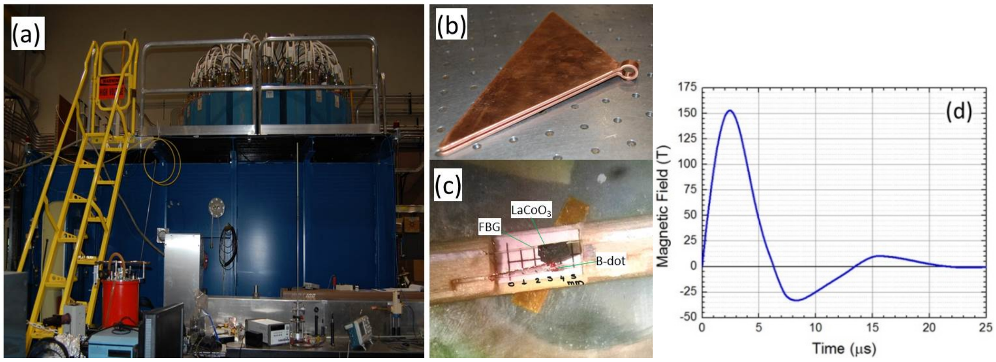

Fig. 4 Photograph of the NHMFL single-turn coil pulsed field facility is shown in (a). Current (4.5 MA) from the capacitor bank is delivered to a target coil (shown in (b)) using a triangular shaped pair of parallel plate OHFC copper conductors that serve as the supply and return current transmission lines. Millimeter sized experiment samples are loaded onto a wooden dowel with a magnetic field B-dot sensor and 1-mm long FBG sensor as shown in (c). (d) Magnetic field waveform for the NHMFL single-turn system as measured by the *in-situ* B-dot probe.

Two types of materials were studied using the 100 MHz coherent pulse FBG interrogator system. The first was the quantum paramagnet $SrCu_2(BO_3)_2$ and the second sample was the insulating perovskite cobaltite $LaCoO_3$ (LCO). FBG dilatometry in both of these systems have been benchmarked using the slower motor-driven-generator field to 100 T with a multi-channel spectrometer approach [18,19] with a linear diode (InGaAs) array readout at 47 kHz. The results here represent our first preliminary studies on the capacitor-driven single turn coil to 150 T. Here we briefly discuss our results for LCO only. The FBG wavelength shift ($\Delta\lambda$) with applied field for LCO is plotted in Fig. 3. A zoomed in plot of the LCO results showing the magnetic field and FBG wavelength shift versus time shows the critical times of interest for detection of field induced spin transition and resulting crystal magnetostriction is shown in Fig. 5(a). After peak field at 2.5 μs on the down sweep side of the magnetic pulse, the FBG data does not show the reversibility that typically appears in magnetostriction data once the field is removed. Instead, it appears as if the FBG signal becomes dominated by a magnetic impulse driven damped acoustic wave that damps out over the full time scale of 50 μs (Fig. 3). This is better illustrated with the plot in Fig. 5(b) where the magnetostriction strain (i.e., $\Delta L/L = \varepsilon_z$) versus magnetic field is shown. The transition occurring at just above 60 T is in agreement with previous observations of a first order phase transition in LCO [19]. The data also suggests that there is possibly a second transition occurring in the 110-125 T range, which would be consistent with some data published on magnetization of LCO in explosive-driven pulsed power experiments [24]. The field upsweep (red portion of trace in Fig. 5(b)) shows more clearly these transitions. However, the down sweep (blue portion of trace in Fig. 5(b)) shows that the observed transitions did not reverse, and we surmise that the FBG may have become detached from the sample after peak field, or that the magnetic impulse may have introduced an acoustic pulse that rendered a compromised magnetostriction measurement after peak field. Although the full interpretation of the magnetostriction strain results are beyond the scope of this paper, we emphasize the success of the coherent pulse FBG interrogation system's ability to time-resolve strain dynamics with speeds that are well beyond FBG interrogation systems in the field today.

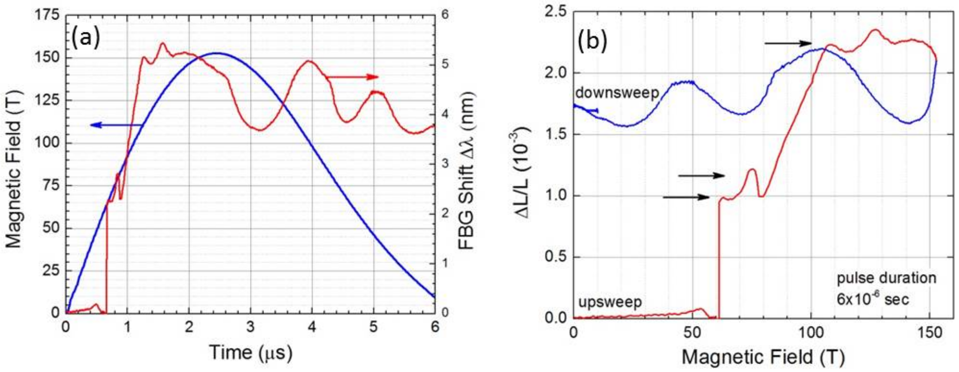

Fig. 5. After a zero time correction to the FBG data time axis, a zoomed in plot of processed coherent time domain FBG waveform data and the main 6 μs quarter cycle time window where magnetic field is strongest and before field reversal occurs is shown in (a) for the $LaCoO_3$ experiment of Fig. 3. A plot after converting to magnetostriction strain (ΔL/L) versus magnetic field allows identification of the magnetic spin induced phase transitions observed (indicated with black arrows) is shown in (b). The magnetic pulse duration period of interest is 6 μs with the upswept portion of the field in red and the down swept part in blue. The irreversibility of the measurement is seen as the upsweep and downsweep portions are not mimicked.

### *3.2 Pressure: fiber Bragg sensing in thermal ignition of high explosives*

In addition to strain, we use FBG sensors to perform stress measurements. Over the last few years we have reported on various approaches [5,6,8] to make high-speed pressure measurements using FBGs under conditions of shockwave loading in inert materials from impact experiments. Here we report on complementary pressure measurements using the coherent pulse FBG interrogation system in thermally ignited high explosives. From a safety perspective, an improved understanding of thermal explosions is needed for setting standards on handling, storage, and transportation in the prevention of and response to possible accidents such as fire. Measurements of state variables pressure, temperature, and density, are needed to validate models of the thermal response of high explosives [25]. With a rate dependent measurement of these quantities, a measure of the energy release rate which determines reaction violence is obtained. Over the last few years, several important complementary diagnostics have been developed to extract some of the mentioned quantities in these experiments, these include IR thermometry and thermocouple measurements for temperature [26] and penetrating radiography for density and material flow rates [27–29]. However, the one elusive quantity that has been difficult to measure is pressure because of high temperatures and material flow that occurs during the sub-sonic blast. Previous methods have included carbon resistive and manganin foil gauges with some success [30], but in general, an FBG based sensor is attractive because of its unobtrusive small diameter and noise free isolation from other electrical based diagnostics.

A schematic and photograph of the experimental package assembly is shown in Fig. 6. Further details on the experimental package can be found in Refs [28,29]. A pair of 12.5 mm diameter right cylinder pellets of the plastic bonded explosive PBX 9501 (HMX 95%; Estane 2.5%; BDNPA-F 2.5%) is used for these measurements. The pellets are stacked on top of each other so that midplane diagnostics (IR fiber pyrometry and thermocouples) can be placed in the center volume portion of the assembly as in Fig. 6(b). The high explosive (HE) pellets are housed in an end-capped aluminum sleeve. The end caps are held in place with bolts as shown in Fig. 6(a), and an initial small gap between the pellets and the aluminum case allowed for material volume expansion as the high explosive is heated The HE is heated by a set of thin film resistive heaters attached to the case. Fig. 6(c) illustrates the locations of the additional diagnostics. Thermocouples are used to independently monitor the temperature, and IR fiber pyrometry measures heat and light emission from the HE at the onset of ignition. Dynamic x-ray radiography [29] is used to measure density changes and material flow during the final critical tens of microseconds leading to ignition and following the subsequent burn propagation. The radiography interframe time was 5 microseconds. A single 1-mm-long 1560 nm FBG is embedded into the HE. The FBG was written on polyimide coated SMF28 fiber, and the grating was recoated after the grating is written to avoid breakage at the grating section.

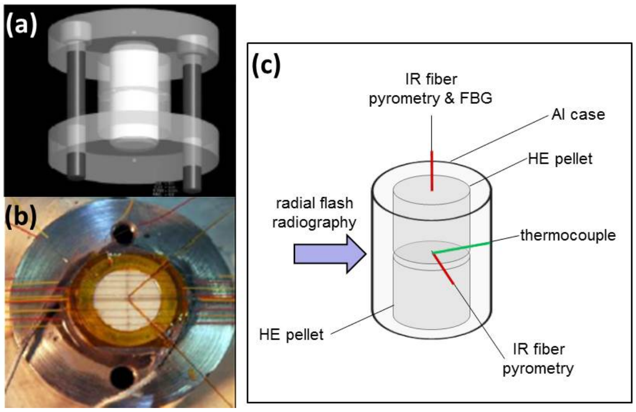

Fig. 6. (a) Schematics, and (b) photograph, showing the relative sizes and location of the aluminum case and encased high explosive pellets. In (b), the midplane section between two pellet halves is shown to expose the placement locations of the array of thermocouples and a pair of IR pyrometer optical fibers originating from the center. The illustration in (c) shows the relative placement locations of all the diagnostics: FBG, thermocouples, pyrometer fibers, and x-ray flash radiography.

Experiments initially proceed by heating the sidewalls slowly over the period of 1.5 hours. Internal temperature measurements are continuously recorded using the signal from thermocouples with a computer controlled voltmeter, but since the FBG also responds to temperature, continuous recording of the FBG wavelength shift versus temperature is also done using the time integrating InGaAs array spectrometer (see Fig. 1). Thermally driven explosion experiments proceed by monitoring observables (usually internal HE temperature) over the course of the heating phase from which real time indicators in temperature are able to track subtle changes such as material phase change and HE chemistry induced self-heating effects. These indicators yield a measure of thermal decomposition before internal chemical reactive kinetics give way to a full self-sustaining explosion with ignition and burn propagation. Thermal decomposition occurs over time scales of hours. As exothermic chemistry begins, the material self-heats and the decomposition accelerates. This causes a thermal runaway which leads to the thermal explosion. Final steps in the development of a thermal explosion are observed via temperature and density to evolve on the time scale of seconds. Ignition then occurs and a switch in energy release to post-ignition time scales of microseconds is observed. Post-ignition burn propagation occurs for a duration of tens of microseconds and during this phase, extreme temperatures and pressures generated cause many probes to fail. This is where the FBG sensor interrogation speed becomes paramount. In Fig. 7 we plot the temperature time history of a thermal ignition event for PBX 9501. Plotted alongside the thermocouple data is the FBG data as recorded by the InGaAs spectrometer. Note the similarities in signature between the thermocouple data and the FBG data. The temperature was temporarily held at a couple of intermediate points (70° C, 175° C) before being held fixed at the final temperature of 205° C. At the 175° C point, the temperature is held to allow for material flow and rearrangement as the HMX undergoes a volumetric expansion due to the $\beta \rightarrow \delta$ crystalline phase transition. FBG data is subject to pressure as well as temperature, and during the he $\beta \rightarrow \delta$ phase change there was a slight temperature drop due

Received 7 Apr 2015; accepted 18 May 2015; published 21 May 2015

to the endothermic phase change and commensurate with a volume expansion that slightly increased the pressure causing the FBG shift to lower wavelength. At the final hold temperature of 205° C, reactive self-heating in the HE occurs in the final 1000 seconds before a full ignition. Post triggering of the oscilloscope is used to record the final ignition event and explosively driven pressure build up in the package using the coherent pulse FBG interrogation system for the final 1 millisecond before the aluminum case containment fails and breaks up. Temperatures recorded during runaway to ignition are in the ~250° C range. We use this information to feed the analysis of the FBG signal since the multi-parameter response of FBGs to pressure and temperature leads to some uncertainty in the pressure measurements.

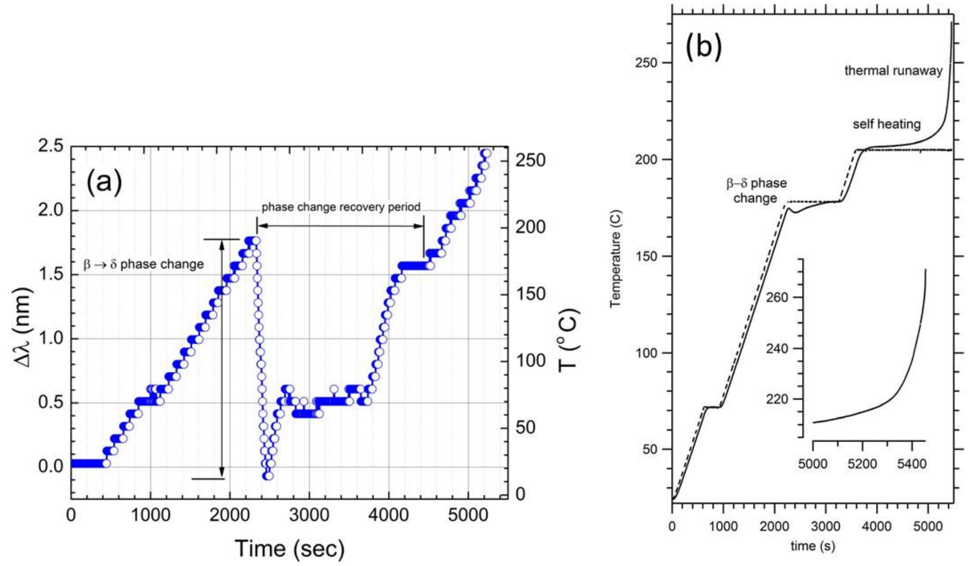

Fig. 7. A plot of the FBG wavelength shift (Δλ) versus time for thermally heated PBX 9501 before ignition is shown in (a). The initial wavelength of the FBG was λ=1555.1 nm, and the corresponding temperature is given on the right ordinate labeled axis using a wavelength shift to temperature conversion constant of 11 pm/°C. The FBG data in (a) is, for a period during the heating phase, disrupted by the β→δ material phase change that results in volume expansion and stress effects on the FBG response after t = 2200 sec. In (b), a plot of the thermocouple data for heated PBX 9501 (taken from Ref [29].) is shown. The dashed plot in (b) represents the aluminum case temperature history, and the solid line is the temperature measured at the center of the PBX 9501 cylinder. Best agreement between the FBG and thermocouple data is before the phase change period and well after the phase change recovery time when self-heating of the explosive begins to produce thermal runaway in excess of 205° C.

Ignition of the explosive is precipitated by thermal runaway after a short period of self-heating (Fig. 7(b)). The FBG response during ignition breakout and propagation is recorded by the coherent pulse FBG interrogation system for ~500 μs, the total recording window of the digitizing oscilloscope, until the aluminum case breaks. A break foil on the aluminum case serves as a post trigger for the digitizer. In all tests to date, we observe an FBG time domain signal dominated by a shift to shorter wavelengths (pressure). The pressure shift dominates any apparent shifts to longer wavelengths due to temperature. In Fig. 8 we plot the FBG wavelength shift (Δλ) for a thermal ignition experiment in PBX 9501. Time zero is the time instant when the break foil on the aluminum case triggers the oscilloscope and coincides with breakup of the case. The data shows a continuous shift to shorter wavelengths for all times until failure of the sensor at t = -44 μs. For all time in the plot of Fig. 8 (and for data not shown in the plot), -410 μs ≤ t ≤ -44 μs there is no red shift in the FBG wavelength. The late time dynamics have consistently shown an FBG wavelength shift dominated by the blue shift to shorter wavelength from pressure. This does not absolutely rule out a temperature increase

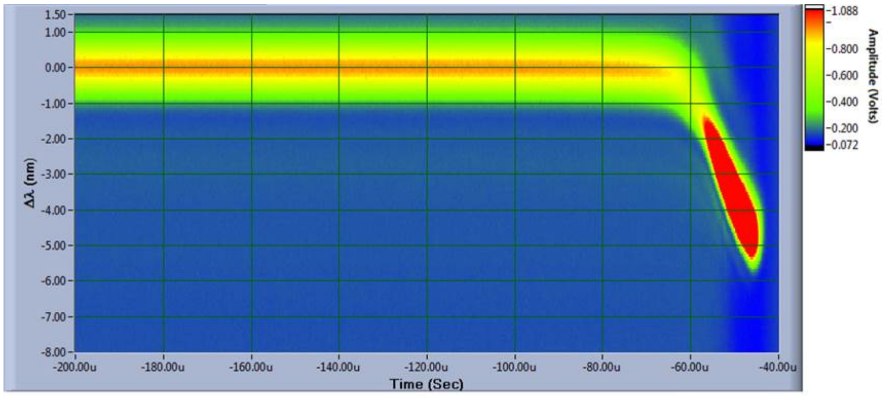

Fig. 8. Plot of the processed coherent time domain FBG waveform data, from a thermal ignition experiment, in the PBX 9501 explosive. The 1-mm-long FBG grating center wavelength was 1559.9 nm before heating (room temperature). Just before thermal runaway, the FBG center wavelength was 1563.7 nm.

that may be embedded as a small negative contribution in the pressure rise portion of the signal. However, a reasonable estimate of the pressure was made by eliminating the contribution from temperature offset present at the beginning of the coherent pulse FBG time waveform. This is shown in Fig. 9. At room temperature (i.e., before any heat was applied) we measured the time domain spectrum of the 1560 nm FBG grating using the conversion factor of time to spectrum knowing the following: initial FBG center wavelength (1559.89 nm), the full chromatic dispersion length of the fiber (33.068 km), and the dispersion factor of 0.0167 ns/(km-nm). Figure 9(a) shows that the FBG at room temperature is centered at λ=1559.89 nm, and on the time axis, it peaks at time shift of Δt=0.74 ns when compared to the laser clock pulse. Then, after the PBX 9501 explosive has been heated and held at 205° C, thermal run away occurs followed by ignition. In Fig. 9(b) we plot the time domain FBG spectrum and laser clock at a time early in the ignition/heating phase (t ~ -410 μs), and note that the time shift between these two pulses is now Δt=2.84 ns showing an increase in the FBG to longer wavelength, λ=1563.7 nm. This λ shift from the room temperature measurement corresponds to a temperature shift to T=338° C, assuming a temperature shift FBG coefficient of 0.012 nm/°C. From the data in Fig. 8, we see no further increase in the FBG wavelength due to temperature, and in Fig. 9(c) we plot the FBG time waveform at t=-45.017 μs where pressure buildup from the resulting blast wave blue shifts the FBG wavelength from an early time (t=-410 μs) value of 1563.7 nm to a late time (t=-45 μs) value of 1559.1 nm. A pressure time history for the given experiment is shown in Fig. 9(d). The pressure is seen to rise monotonically to peak value of 1.22 GPa before the FBG sensor fails at t=-43.6 μs. The pressure build-up dynamics is relatively slow (compared to a shock wave pressure profiles [5–7]), and we treat the FBG response as quasi-hydrostatic allowing us to use the hydrostatic pressure shift coefficient of -4 pm/MPa to calibrate the pressure with respect to FBG wavelength shift. During this pressurization period, it is not possible to determine the additional contribution from temperature, however, we believe our early time estimate of temperature and resulting peak pressure is consistent with measurements based on carbon resistor gauges [30]. Variability in the PBX 9501 pressure measurement is expected, and after performing a series of experiments, we plot the summary of the extracted pressure in Fig. 10 for five experiments. The data for five experiments shows that there is variability in the shape of the pressure wave profile. The data, however, is consistent with showing a pressure dominated response that begins in the vicinity of t=-70 μs to t=-55 μs that continues to show a

#237107 - $15.00 USD Received 7 Apr 2015; accepted 18 May 2015; published 21 May 2015

pressure increase for an additional period of ~30 μs rising to a peak pressure in a range of 1.2 to 2.0 GPa. The data in Fig. 10 are consistent with expected FBG pressure impulse time using a burn velocity estimate from x-ray radiographic measurements of material flow during the event [29] and from pressure measurements using carbon resistor probes [30]. Variability in the shape is attributed to changes in the initial position of ignition which can occur in regions outside of the midplane region of the explosive with extended non-point like density gradients [28,29]. The other possible source of variability in the data can also be from the FBG and its response to dynamic pressure impulses from the explosive blast. A study to address these issues may be necessary to determine the effects on FBG response. Nonetheless, despite these difficulties, the value of bounding the pressure buildup range in these types of experiments are of value and were achieved using the high-speed FBG interrogation approach presented here. Further development work for FBG pressure extraction in thermal explosion of high explosives is warranted.

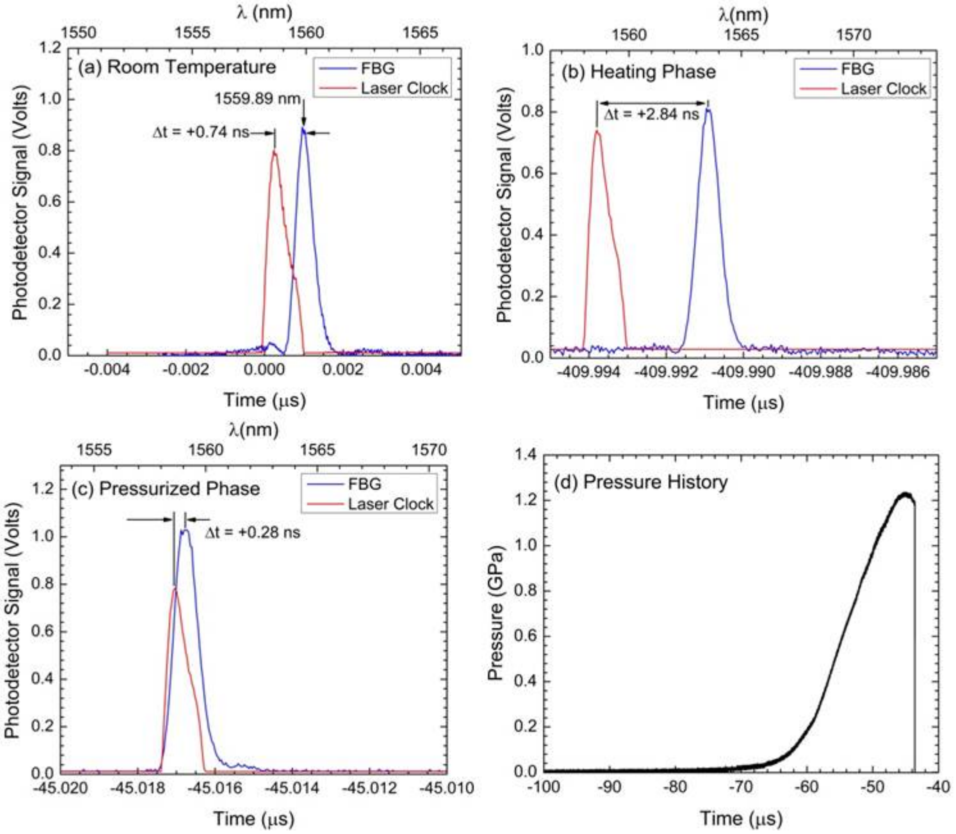

Fig. 9. The plots in panels (a) thru (c) are small 10 ns time slice windows of the coherent pulse FBG time domain waveform for a thermal ignition experiment in PBX 9501. In each panel the FBG (blue trace) and laser clock (red trace) are shown. Conversion to wavelength and λ-shift is done by using the corresponding measured time shift, dispersion fiber length (33.068 km), and dispersion coefficient (0.0167 ns/(nm-km)) for the fiber. The traces in each panel are the (a) room temperature – i.e., preheat phase, (b) early heat phase at t≈-410 μs, and (c) pressurization phase t≈-45 μs in a PBX 9501 thermal ignition experiment. The final panel (d) is the pressure history profile for the entire data set from the FBG time domain waveform of Fig. 8. A monotonic increase in pressure dominates the FBG response between 70 μs ≤ t ≤-43.6 μs.

#237107 - $15.00 USD Received 7 Apr 2015; accepted 18 May 2015; published 21 May 2015

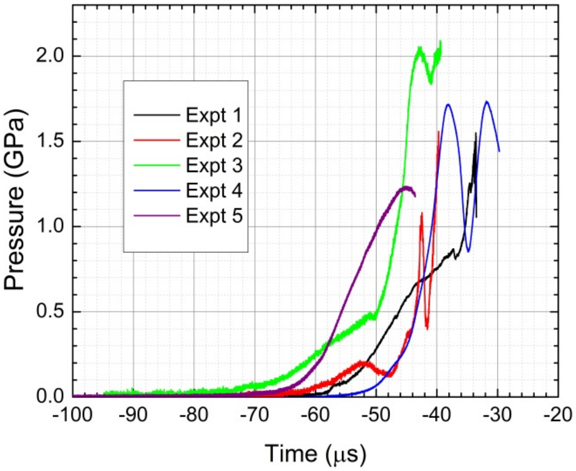

Fig. 10. A data set of five FBG measured thermal ignition pressure measurements in PBX 9501 is shown. Differences in the pressure profiles are attributed to variability in the initial position of the ignition flash point, flow, and from FBG sensor response.

## 4. Discussion

We introduced a coherent pulse FBG interrogation method capable of 100 MHz readout rates with the ability to sense strain and pressure at speeds necessary for resolving dynamic events occurring at the microsecond time scale, where nanosecond level time resolution is required. The FBG interrogation system was applied to the detection of strain and pressure in material dynamics where traditional FBG interrogation approaches (i.e, multichannel spectrometry using arrayed detection, frequency swept lasers, etc.) are too slow for resolving the FBG sensor wavelength shift under impulse loading conditions. In a number of applications, the coherent pulse FBG interrogation approach provides affordable speed and spectral resolution that can be tailored to specific needs. In its current configuration, the interrogation update rate is equal to the laser repetition rate that provides a 10 ns (1/100 MHz) readout update time. The spectral resolution is determined by the combination of photodetector bandwidth, effective chromatic dispersion, and recording sampling speed of the oscilloscope. In our example, we typically used enough chromatic dispersion to constrain the expected (and observed) FBG wavelength shift within one laser clock period of the modelocked fiber laser. The effective number of wavelength points in a 10 ns time window is 500 points using a 50 GS/sec 25 GHz sampling oscilloscope, but the Nyquist limit (25 GHz) in terms of resolution is 250 points. For the magnetostriction strain measurements we used 100 km of fiber dispersion which yields a spectral resolution of 24 pm at the Nyquist limit. In this approach, the only alternative to maintain very high spectral resolution over a large spectral observation band is to increase the speed in the detection components or to reduce fiber laser repetition to say 50 MHz using a fiber pulse picker. If the repetition rate is reduced to 50 MHz, then the new clock period of 20 ns becomes the allowable window for performing the spectral dispersion. This should be adequate to doubling the resolution provided the reduced interrogation rate of 50 MHz is sufficient to resolve the dynamics.

Another important aspect to the FBG interrogation system is the sensor response to the various stimuli: strain, stress, and temperature. Often FBG sensors are packaged in various configurations that allow for attaching the FBG suitable for placement of the transducer in ruggedized housings. However, in the situation where fast time response for dynamical measurements is paramount, one must use bare FBGs in direct contact with the material. For the magnetostriction measurements presented, attaching the FBG sensor to the sample under test with epoxy has proven to be sufficient [9,18,19]. However, in our example of determining pressure driven by a sufficiently slow high explosive burn front, the results are much more

Received 7 Apr 2015; accepted 18 May 2015; published 21 May 2015

difficult to uniquely determine. This is especially true for processes where both pressure and temperature are present and the FBG is responding to both influences. In our thermal explosion example above, we can only partially compensate for this effect, and at best, our measurements are still estimated measures. Deconvoluting the effects from multi-parameter harsh environments with FBG sensing is still an ongoing research topic, and several approaches using clever probe designs with side-hole, polarization maintaining, sapphire, hollow core, structured fiber tips have been proposed to reduce the sensitivity of the sensor from one parameter (i.e., stress versus temperature) compared to another. Although these results represent studies using an interrogation approach to increase speed, we are currently designing a future system to tackle the same issue using a coherent pulse interrogation scheme as described here.

## 5. Conclusions

In conclusion, a 100 MHz fiber Bragg grating interrogation system to measure dynamic strain and pressure has been developed. This technique is especially useful for measuring material dynamics at high speed under conditions of extreme loading from impulse driven events. We demonstrate two applications of FBG based strain and pressure measurements where single-shot *in-situ* interrogation speed on the 10 ns scale is necessary for resolving material response under impulse loading on the microsecond scale. Application to pulsed-power magnet driven magnetostriction in the magnetic materials demonstrated strain measurements, and pressure measurements in thermal ignition events in high explosives were also demonstrated. The approach should find use in situations where extreme pressure and/or strain detection speeds are necessary. The approach can be generalized to other types of FBG sensors such as distributed arrays or chirped FBGs should one require a measure over an active length of hundreds of mm that can be used in shock or detonation wave tracking and detection.

## Acknowledgments

This work was supported by the DOE/NNSA Laboratory Directed Research and Development program at Los Alamos National Laboratory under the auspices of the U.S. Department of Energy for Los Alamos National Security, LLC, Contract No. DE-AC52-06NA25396. We would like to thank Dwight G. Rickel, Ross D. McDonald, Jon B. Betts, and Andreas V. Stier for their technical support at the NHMFL. The National High Magnetic Field Laboratory Pulsed Field Facility is supported by the National Science Foundation (NSF), the US Department of Energy (DOE), and the State of Florida through NSF Cooperative Grant DMR-1157490. Work at LANL was supported by the US DOE Basic Energy Science project "Science at 100 Tesla."